Diagnosing the development of seasonal stratification using the potential energy anomaly in the North Pacific

Ryohei Yamaguchi, Toshio Suga, Kelvin J. Richards & Bo Qiu

Climate Dynamics
Observational, Theoretical and Computational Research on the Climate System

ISSN 0930-7575

Clim Dyn
DOI 10.1007/s00382-019-04816-y

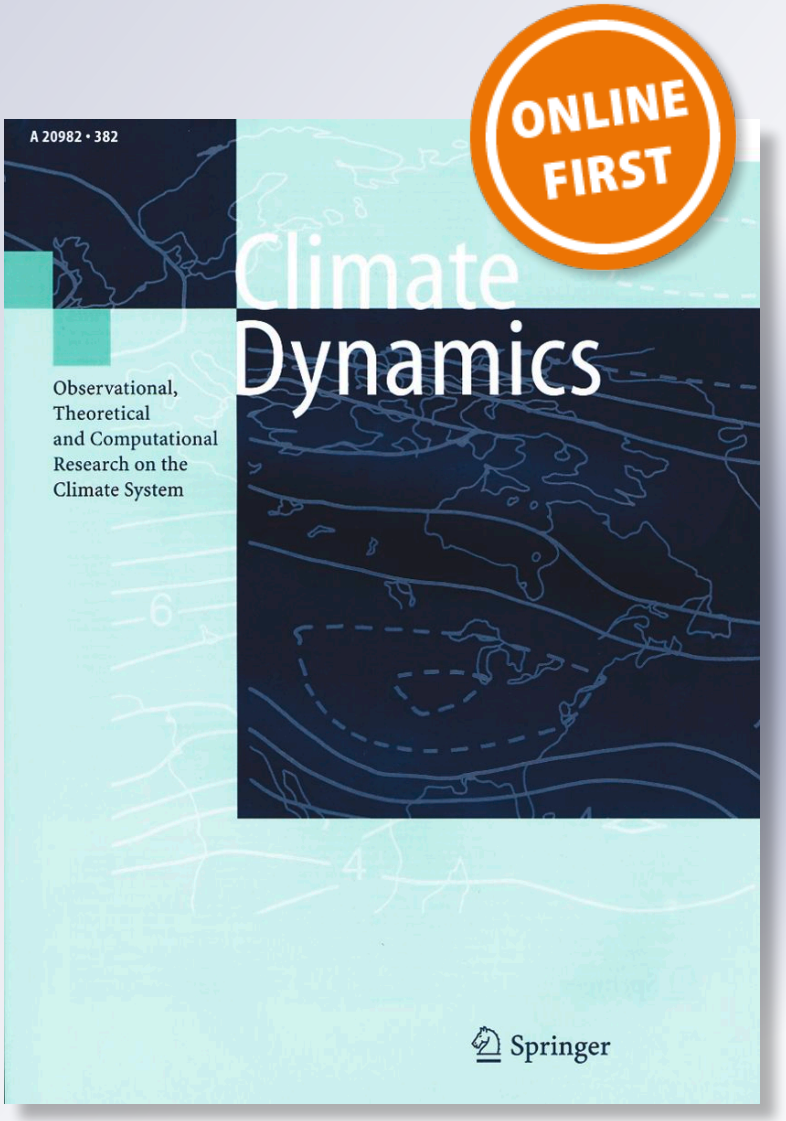

Springer

Climate Dynamics
https://doi.org/10.1007/s00382-019-04816-y

Diagnosing the development of seasonal stratification using the potential energy anomaly in the North Pacific

Ryohei Yamaguchi[1] · Toshio Suga[1,2] · Kelvin J. Richards[3] · Bo Qiu[4]

Received: 8 January 2019 / Accepted: 9 May 2019

Abstract
Upper-ocean seasonal stratification (seasonal pycnocline and/or transition layer) is a ubiquitous feature and its vertical structure has large spatial variability. The density stratification regulates the stability of the upper ocean and thus can affect the oceanic response to atmospheric forcing and biogeochemical processes by modulating vertical mixing. In this study, we described the development of the seasonal stratification in terms of the stability of the water column, using the potential energy anomaly (PEA) as a metric based on Argo profiles. PEA budget analysis reveals that over most of the North Pacific, seasonal stratification develops under a vertical one-dimensional energy balance between an increase in PEA (i.e., a strengthening of the stratification) driven by atmospheric buoyancy forcing and a decrease in PEA associated with vertical mixing within the water column. Horizontal advection of PEA plays a significant role in the seasonal development of the stratification only in the regions of the western boundary current and equatorial current system south of 10°N. We find that, in addition to the total magnitude of the oceanic buoyancy gain, the balance between compositions of the atmospheric forcing (non-penetrating surface buoyancy forcing and penetrating radiative heating) is also important in explaining regional differences in the development of the seasonal stratification. The vertical diffusivity in the seasonal stratification estimated from the residual of the PEA budget is in the range from 5×10^{-5} m^2 s^{-1} to 5×10^{-4} m^2 s^{-1} and shows spatial and seasonal variability associated with local wind forcing.

1 Introduction

The upper ocean in the warming season consists of a relatively thin mixed layer (ML) and seasonal stratification (seasonal pycnocline and/or transition layer) below the ML. Seasonal change in stratification is a ubiquitous feature of the North Pacific. In the warming season, the stratification develops as a result of heating, freshwater supply and wind forcing from the atmosphere, and oceanic lateral processes. While the development of a seasonal stratification occurs across the North Pacific, its vertical structure differs regionally (Fig. 1). For example, shallower and sharper seasonal stratification tends to develop in the northern part of the North Pacific compared to the southern part. In the Kuroshio and its extension regions, a more substantial buoyancy gain occurs in the subsurface, leading to stratification with more linear vertical structures. These features are the result of regional differences in the dominant processes of forming the seasonal stratification.

Heat, freshwater, momentum, and chemical tracers exchanged between the atmosphere and ocean are transported into the ocean interior through the ML and the seasonal stratification. Since the seasonal stratification characterizes "difficulty in mixing (i.e., stability)" of the upper ocean due to its maxima in the density stratification, it has great potential of influences on physical and biogeochemical processes within the upper ocean.

Vertical mixing below the ML during the warming season is controlled by the strength of stratification (Qiu et al. 2004; Cronin et al. 2013). In turn, this can affect the supply of nutrients from the subsurface and the vertical transport of heat, which is an important factor in determining the sea

✉ Ryohei Yamaguchi
ryohei@pol.gp.tohoku.ac.jp

[1] Department of Geophysics, Graduate School of Science, Tohoku University, Sendai, Japan

[2] Research and Development Center for Global Change, Japan Agency for Marine-Earth Science and Technology, Yokosuka, Japan

[3] International Pacific Research Center, University of Hawaii at Manoa, Honolulu, HI, USA

[4] Department of Oceanography, University of Hawaii at Manoa, Honolulu, HI, USA

Published online: 20 May 2019

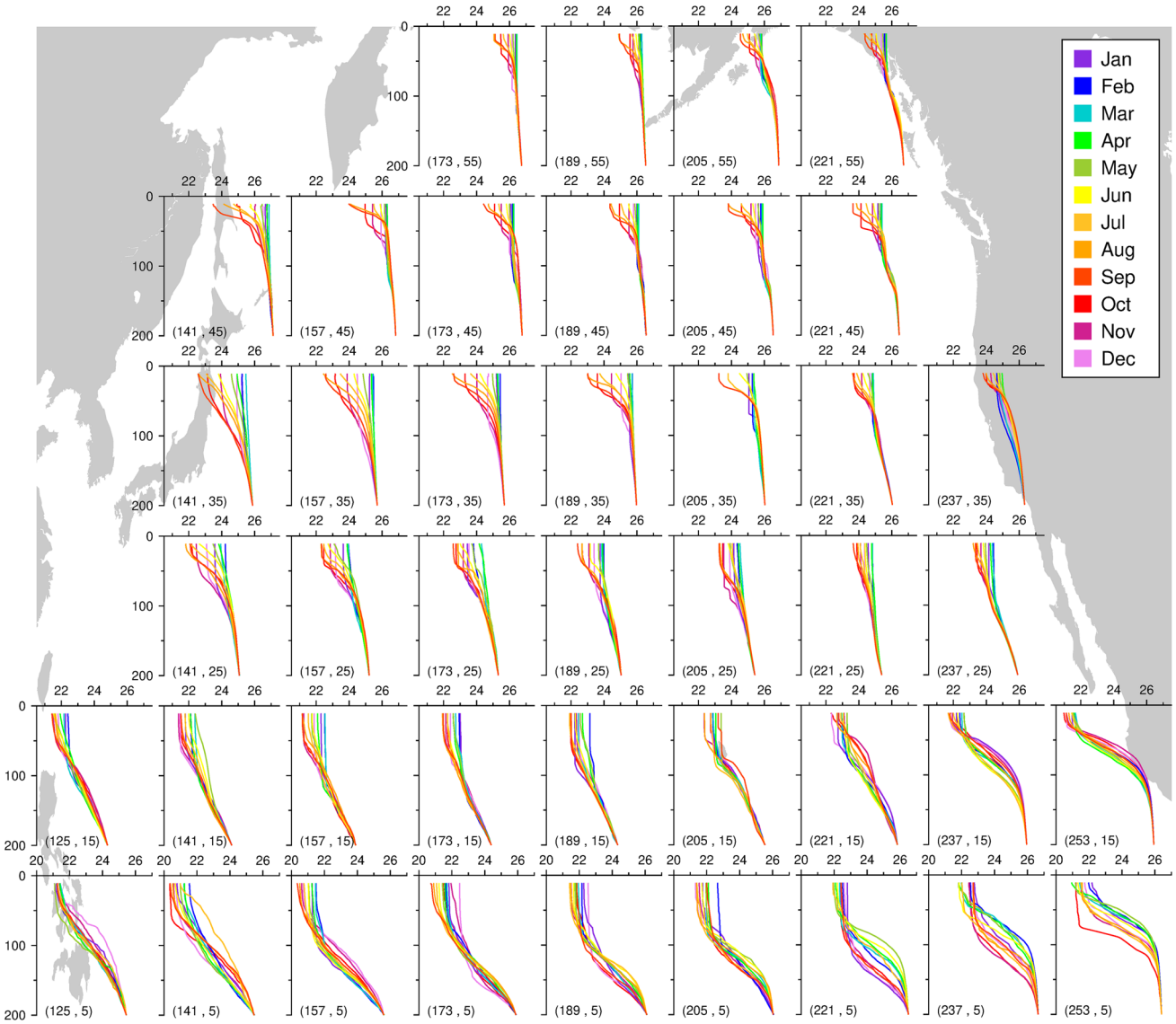

Fig. 1 Seasonal cycle of the upper-ocean potential density stratification in the North Pacific, based on Argo data sampled during 2006–2016 (y-axis: depth (m), and x-axis: potential density (kg m^{-3})]. Profiles are averaged over a 2° (longitude) × 2° (latitude) region centered at labeled location [longitude (°E), latitude (°N)]. Averaged profiles are normalized to the potential density at 200 m in February following the procedure of Moisan and Niiler (1998)

surface temperature during the warming season (Hosoda et al. 2015). Moreover, not only in the warming season, the upper ocean stability that develops during the warming season can also affect ocean ventilation via its impact on the development of the winter ML (e.g. Qiu and Chen 2006; Kako and Kubota 2007). Despite the importance of seasonal stratification for physical and biogeochemical processes, the formation and spatial variability of seasonal stratification have not been widely investigated from an observational perspective (e.g., Johnston and Rudnick 2009).

Previous model and observational studies have used common metrics to quantify upper ocean stratification. These include the density or temperature difference between the surface and subsurface, and the buoyancy frequency (e.g. Tomita et al. 2010; Capotondi et al. 2012; Maes and O'Kane 2014). While these metrics are useful, being readily obtained from low vertical resolution observational data or climate model output, they do not always quantify the "difficulty in mixing", which is the essence of seasonal stratification. To assess the influences of seasonal stratification on biogeochemical processes and air-sea interaction, a metric capable of quantitatively representing this "difficulty in mixing" of the water column is needed.

In this study, for a metric, we used the potential energy anomaly (PEA; ϕ) advocated by Simpson (1981). PEA

defined from the surface ($z = 0$) to the base of a depth ($z = -H$) is written as;

$$\phi = \frac{1}{H}\int_{-H}^{0} (\bar{\rho} - \rho)\, gz\, dz = -\frac{1}{H}\int_{-H}^{0} \tilde{\rho} gz\, dz, \tag{1}$$

with the vertically averaged potential density being written as

$$\bar{\rho} = \frac{1}{H}\int_{-H}^{0} \rho\, dz,$$

where $\tilde{\rho}$ ($=\rho - \bar{\rho}$) is the deviation from the vertically averaged potential density and g ($=9.80$ m s^{-2}) is the acceleration due to gravity. PEA provides a measure of the amount of energy per unit volume (J m^{-3}) required to make the density stratified water column vertically homogeneous; it, therefore, directly represents the "difficulty in mixing". Examples of calculation of PEA are shown in Fig. 2. Using this PEA as a metric, together with its time-dependent equation, we are able to discuss quantitatively the development and spatial variability of the seasonal stratification in terms of stability.

Making use of observational data, the purpose of this study is to describe the development of seasonal stratification in terms of "difficulty in mixing", and to discuss the dominant processes forming the stratification and their balance using a time-dependent equation for PEA. We also examine the effectiveness of applying the PEA budget analysis, which has generally been used in studies of coastal studies, to the seasonal stratification in the open ocean.

The remainder of this paper is organized as follows. In Sect. 2, the dataset and the processing methods are described. The PEA climatological field and its seasonal cycle are described in Sect. 3. In Sect. 4 we outline the configuration and validation of the PEA budget analysis and the results of the PEA budget. In Sect. 5 we discuss the difference in the balance of terms in the budget, demonstrating three representative regions as the examples. Finally, a summary is provided in Sect. 6.

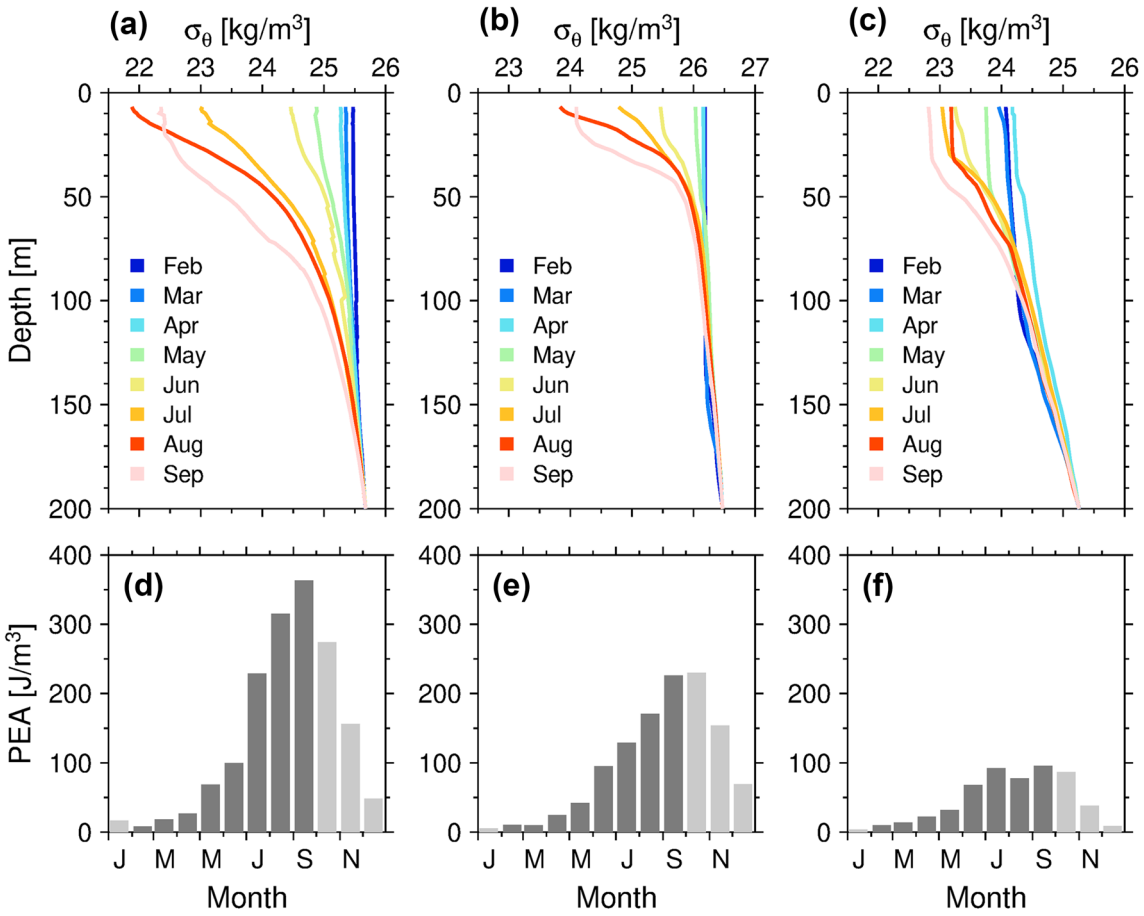

Fig. 2 Examples of the potential energy anomaly (PEA) calculation. **a**–**c** Seasonal cycle of the upper-ocean profile of potential density stratification at (**a** 153°E, 35°N), (**b** 177°W, 43°N), and (**c** 177°W, 23°N). **d**–**f** Corresponding seasonal cycle of PEA with the annual maxima of ML depth (H) set to **d** 144 m, **e** 163 m, **f** 88 m, respectively

2 Data and methods

We mainly used the Advanced automatic Quality Control Argo data (AQC Argo data; http://www.jamstec.go.jp/ARGO/argo_web/ancient/AQC/index.html) for temperature and salinity profiles provided by the Japan Agency for Marine-Earth Science and Technology (JAMSTEC). AQC Argo data includes the Global Data Assembly Center (GDAC) real-time quality control profiles (Argo 2000), with additional quality controls performed by JAMSTEC. The spatial coverage of the Argo profiles in the North Pacific after 2006 is sufficient for detecting the seasonal cycle of the upper ocean stratification. Profiles collected from January 2006 to December 2016 were used. Due to the scarcity of profiles in the coastal and marginal sea regions, these regions were excluded from subsequent analysis. The vertical resolution of Argo profiles varies depending on the initial setting or/and data transfer method and a part of the profiles has the sampling intervals varying with the depth within a profile. In the profiles used in this study, we confirmed that vertically coarse profiles (those have less than twenty observations or a vertical interval greater than 10 m in the upper 200 m) were only ~ 3% of the total profiles. We also checked the spatial distribution and seasonal change in the monthly climatology of PEA were not affected whether those coarse profiles were used or not.

From the QC'ed profiles by JAMSTEC, a few profiles were excluded because they exceeded three standard deviations of the mean profile calculated for the month and within the 3° (longitude) × 3° (latitude) area. After this QC procedure and the potential density calculation, profiles were vertically interpolated to 1-m intervals using Akima spline (Akima 1970). To obtain the gridded fields of the metrics (e.g., PEA and ML depth) and to avoid the smoothing of vertical structures by the spatial and temporal averaging of profiles, metrics were calculated from the raw profile data. Monthly 1° (longitude) × 1° (latitude) fields for each metric were produced using a weight function that is inversely proportional to the distance from the grid point, following Oka et al. (2015).

To evaluate the contribution of lateral processes to the change in seasonal stratification, we also used the Roemmich–Gilson Argo climatology (RG Argo; Roemmich and Gilson 2009). The dataset was gridded using monthly objective mapping to 1° × 1° horizontal resolution with latitude-dependent decorrelation scales. The dataset has 58 levels in the vertical, with a 10 dbar resolution above 170 dbar and a maximum depth of 1975 dbar. After vertical interpolation, using the same procedure as for Argo profiles, we calculated the geostrophic velocity profile assuming a reference depth of 1975 dbar. Daily averaged gridded QuikSCAT and Advanced Scatterometer (ASCAT) wind stress products made available through the Asian-Pacific Data-Research Center (http://apdrc.soest.hawaii.edu/) were used to obtain the monthly Ekman transport field.

We used three daily mean atmospheric datasets to calculate atmospheric buoyancy forcing. The surface net heat flux, Q_{net}, and its four components (shortwave radiation, Q_{SW}; longwave radiation, Q_{LW}; sensible heat flux, Q_{SH}; latent heat flux, Q_{LH}) are from the Japanese Ocean Flux Data Sets with Use of Remote Sensing Observations 3 (J-OFURO3; Tomita et al. 2018). The J-OFURO3 data are derived using a bulk formula to estimate turbulent fluxes based on parameters observed by multiple satellites and have a spatial resolution of 0.25° × 0.25°. The radiation data were taken from the International Satellite Cloud Climatology Project (ISCCP) and Cloud and the Earth's Radiant Energy System (CERES). For the component of freshwater flux, $E-P$ (evaporation minus precipitation), we used the Global Precipitation Climatology Project ver1.2 (GPCP; Huffman et al. 2001) for precipitation rate and the Objectively Analyzed Air-Sea Flux (OA Flux; Yu et al. 2008) for the evaporation rate. The net surface buoyancy flux, $B = -g(\alpha Q_{net}/C_p\rho_0 - \beta(E-P)S_0)$, was then estimated from the net surface heat and freshwater fluxes, where $C_p\rho_0$ ($=4.09\times10^6$ J °C^{-1} m^{-3}) is the volumetric heat capacity of seawater, S_0 is the sea surface salinity, and α and β are the thermal expansion and haline contraction rates of seawater, respectively. These heat and freshwater flux datasets were averaged over the analytical period to obtain a monthly climatology at each 1° × 1° grid points.

The averaging periods for J-OFURO3 and GPCP data are 2006–2013 and 2006–2014, respectively, based on data availability. Although these averaging periods are shorter than those of the oceanic variables (2006–2016), they do not have an impact on our results from the analyses below. We checked that the results of this study were qualitatively unchanged using a climatology constructed from 2006–2013 Argo data.

3 Seasonal cycle of PEA

Since the focus of this work is the layer of the ocean where the density shows seasonal variation (hereafter, seasonal boundary layer), we set the lower limit in the PEA calculation (H) to the local annual maximum of ML depth. ML depth is defined as the depth at which potential density increases (or temperature differs) from the surface value by 0.125 kg m^{-3} (0.5 °C), following the widely used threshold method (Monterey and Levitus 1997). The surface value is assigned to the value at 5 m depth. The seasonal boundary layer depth, H, was obtained from the monthly ML depth

climatology derived from raw profile ML depths using the above-mentioned mapping method.

The spatial distribution of H used in the calculation of PEA is shown in Fig. 3. The thickness of the seasonal boundary layer has significant spatial variability (Fig. 3). Although H can exceed 200 m (the maximum value is 247 m) in the northwestern part of the subtropical gyre where the ML is well developed in late winter (Suga et al. 2004), H is ~ 100 m south of 20°N and is shallowest in the eastern part of the tropics. In pioneering work using observations to investigate upper ocean heat and freshwater balance (Moisan and Niiler 1998; Giglio and Roemmich 2014), a surface that behaves similarly to a material surface was defined in the subsurface and this surface used as the base in the budget calculation. Since H in this study is defined using a similar procedure to these studies, we regard H as a material surface, at least, in the warming season (i.e., when the net sea surface buoyancy flux is downward and the ML is shallow). Indeed, the material surface defined in fig. 1 of Giglio and Roemmich (2014) has a similar spatial distribution to that of H in this study (Fig. 3).

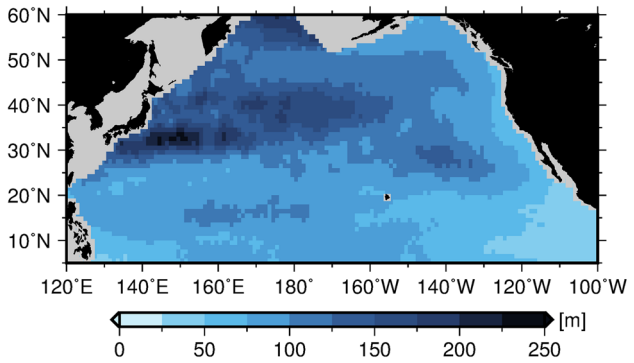

Fig. 3 Spatial distribution of the annual maximum of mixed layer depth (i.e., the seasonal boundary layer depth), H (m)

The monthly climatology of PEA is shown in Fig. 4. PEA has a characteristic spatial distribution that reflects the spatially non-uniform development and decay of the seasonal stratification in the North Pacific. The development of PEA has a latitudinal maximum along 35°N and another local maximum in the eastern part of tropics at ~ 10°N, across a

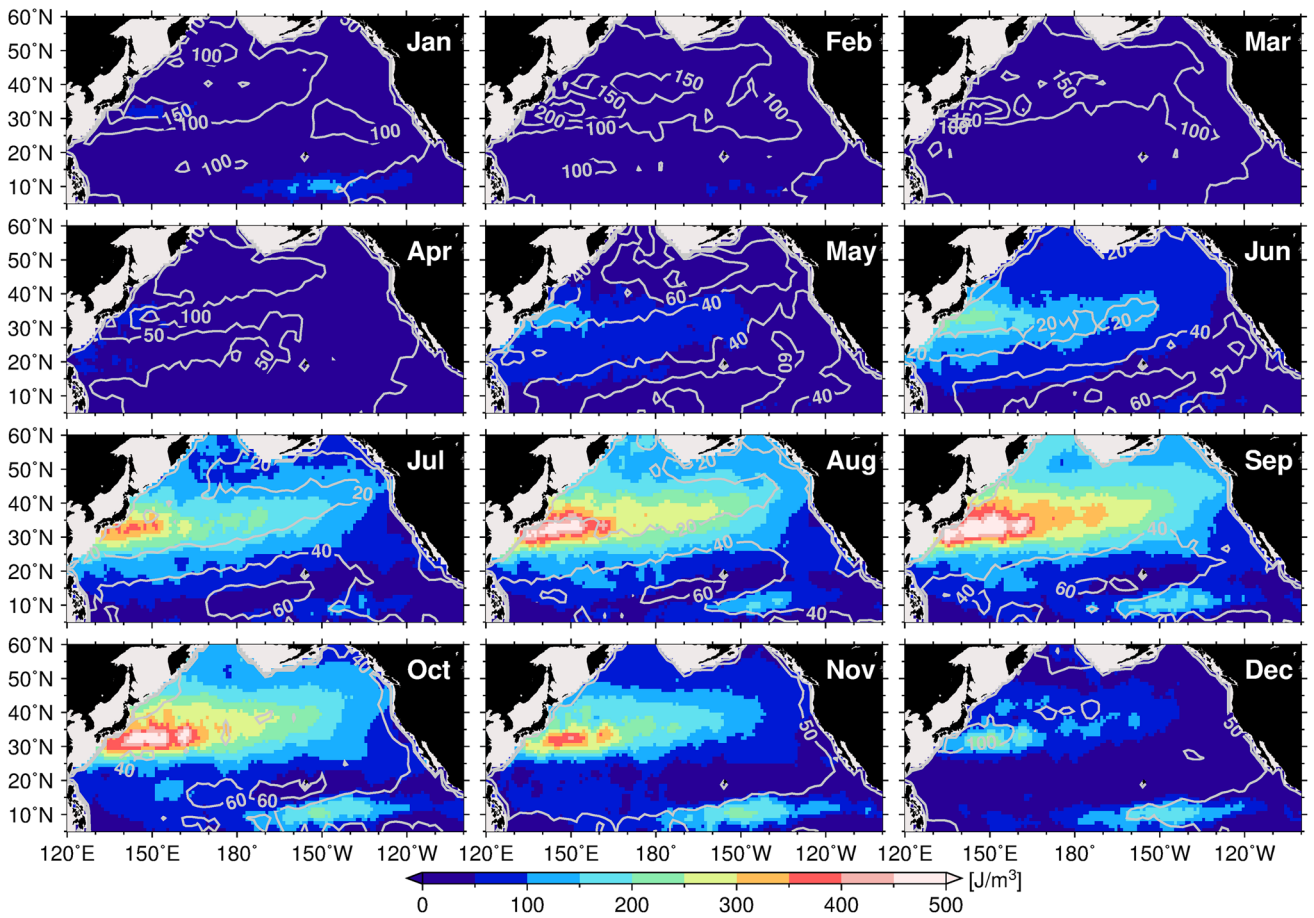

Fig. 4 Seasonal cycle of PEA (J m^{-3}; color) and the mixed layer depth (m; gray contours). The mixed layer depth contour interval is 50 m for November–April and 20 m for May–October

region where the development of PEA is relatively minor. Comparison with the spatial distribution of ML depth reveals that the PEA is larger in the shallower ML depth region during the warming season. However, in late summer (August–September) when PEA is fully developed, the spatial patterns of these two fields do not always correspond. This suggests that PEA development is not determined simply by processes controlling the ML depth under stabilizing forcing during the warming season.

Focusing on seasonal variation in PEA (Fig. 5), the phase of PEA development differs between the high- and mid-latitudes and the tropics. As one might expect, in the high- and mid-latitudes north of 20°N, PEA, which becomes zero by mixing and convection induced by strong cooling and wind forcing during winter, begins to develop in spring and early summer (March–April) and reach its annual maximum stage of development in mid-summer (July–August). In the eastern part of tropics, the phase of PEA development is about 2 months behind that of the mid-latitudes; the PEA starts to develop in May or June and peaks in October or November. At the latitude of 15°–25°N, the PEA develops from spring to early summer in its western part and during late summer in its eastern part, although the changes are relatively small. PEA development lasts around 6 months over the whole North Pacific, although the phase differs among regions. The decay of PEA is a mirror image of the development phase.

It is expected that the surface stabilizing buoyancy forcing is an important factor in the development of seasonal stratification, such as the well-known mixed layer processes under stabilizing forcing. We examined the phase relationship between the development of PEA and the surface buoyancy gain during the warming season. Figure 6 shows the month of maximum development of PEA (Fig. 6a) and the net surface buoyancy gain (Fig. 6b) over the North Pacific, together with their difference (Fig. 6c). The negative values in Fig. 6c indicate that the peak of PEA development precedes that of the net surface buoyancy gain. In many regions of the north of 20°N there is little difference between the phase of their peaks, suggesting that the surface buoyancy forcing plays a dominant role in the development of seasonal stratification in the high- and mid-latitudes. In contrast, significant differences can be seen in regions south of 20°N where the monthly change in PEA is small. This suggests that aside from the surface buoyancy

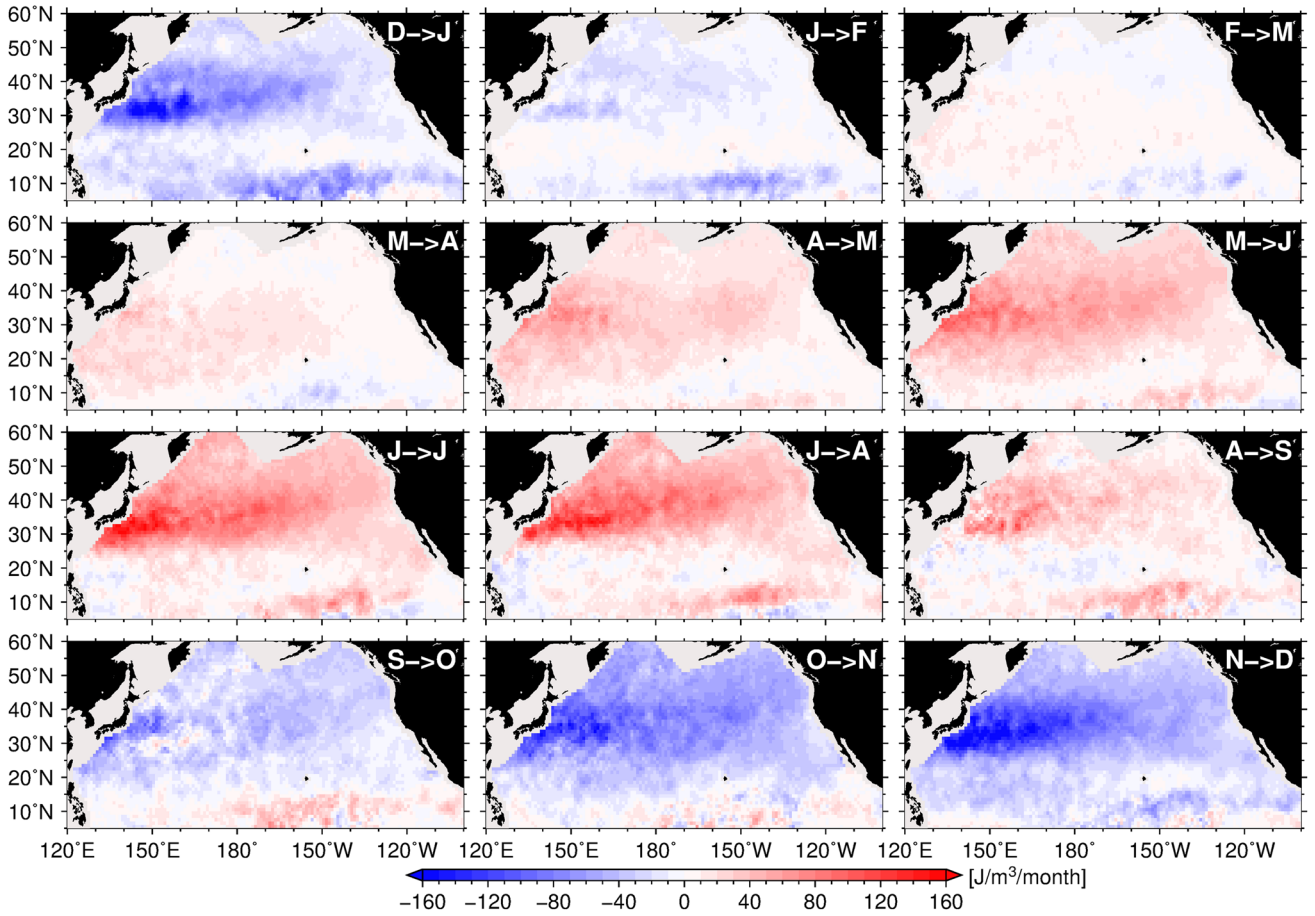

Fig. 5 Maps of the month-to-month change in PEA (J m^{-3} $month^{-1}$). The change is defined as the difference from the previous month

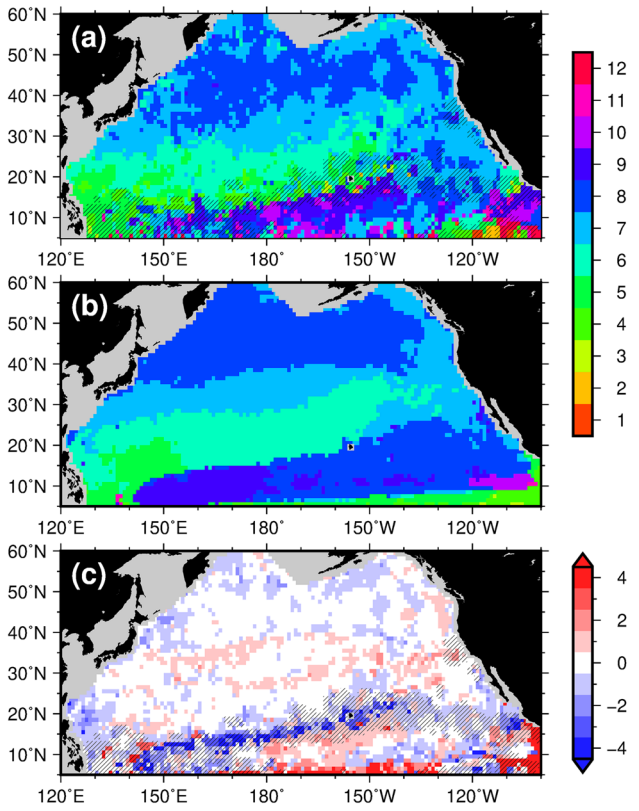

Fig. 6 Month of maximum increase in **a** PEA and **b** net buoyancy gain. **c** Difference between **a** and **b**, (i.e., **a** − **b**). Black hatching indicates regions where the annual maximum of PEA increase is less than 20 J m^{-3} month^{-1}

forcing, other factors, such as lateral processes, contribute to the development of the seasonal stratification in the North Pacific.

4 PEA budget analysis

To quantify the relative contributions of processes driving the development of the seasonal stratification in the North Pacific, we performed a PEA budget analysis using a time-dependent equation for the PEA (Burchard and Hofmeister 2008). Since our focus is the developing phase of the seasonal stratification, we applied the PEA budget analysis to only the warming season (April–August).

4.1 Time-dependent equation for PEA

Burchard and Hofmeister (2008) derived a time-dependent equation for PEA based on the potential temperature and salinity equations, the continuity equation and an equation of state for the potential density. The time rate of change of PEA, defined from the sea surface ($z = 0$) to the annual maximum of ML depth ($z = -H$), can be written as follows:

$$\frac{\partial \phi}{\partial t} = \underbrace{-\nabla_h \cdot (\bar{\boldsymbol{u}}\phi)}_{\langle 1\rangle} + \underbrace{\frac{g}{H}\nabla_h \bar{\rho} \cdot \int_{-H}^{0} z\tilde{\boldsymbol{u}}\, dz}_{\langle 2\rangle} \underbrace{-\frac{g}{H}\int_{-H}^{0}\left(-\frac{H}{2}-z\right)\tilde{\boldsymbol{u}}\cdot\nabla_h\tilde{\rho}\, dz}_{\langle 3\rangle} \underbrace{-\frac{g}{H}\int_{-H}^{0}\left(-\frac{H}{2}-z\right)\tilde{w}\frac{\partial\tilde{\rho}}{\partial z}dz}_{\langle 4\rangle} \underbrace{+\frac{\rho_0}{H}\int_{-H}^{0}P_b dz}_{\langle 5\rangle} \underbrace{-\frac{\rho_0}{2}\left(P_b^s + P_b^H\right)}_{\langle 6\rangle} \underbrace{+\frac{g}{H}\int_{-H}^{0}\left(-\frac{H}{2}-z\right)Q\, dz}_{\langle 7\rangle} \underbrace{+\frac{g}{H}\int_{-H}^{0}\left(-\frac{H}{2}-z\right)\nabla_h\cdot\left(K_h\nabla_h\rho\right)dz}_{\langle 8\rangle}, \tag{2}$$

where $\bar{\boldsymbol{u}}$ is the vertically averaged horizontal velocity vector defined as

$$\bar{\boldsymbol{u}} = \frac{1}{H}\int_{-H}^{0} \boldsymbol{u}\, dz, \tag{3}$$

$\tilde{\boldsymbol{u}}$ is the deviation from the vertically averaged horizontal velocity vector, $\tilde{\boldsymbol{u}} = \boldsymbol{u} - \bar{\boldsymbol{u}}$; $\bar{w}$ and $\tilde{w}$ are the vertical velocity defined by the continuity equation,

$$\nabla_h \cdot \bar{\boldsymbol{u}} + \frac{\partial \bar{w}}{\partial z} = 0, \tag{4}$$

and its deviation, $\tilde{w} = w - \bar{w}$; ∇_h is the horizontal gradient operator; P_b is the vertical buoyancy flux represented as

$$P_b = \frac{g}{\rho_0}K_v\frac{\partial \rho}{\partial z}, \tag{5}$$

with the vertical diffusivity K_v and a constant reference density ρ_0; P_b^s and P_b^H are buoyancy flux at the surface and at the annual maximum of ML depth, respectively; K_h is the horizontal eddy diffusivity; and Q is the source term of potential density,

$$Q = -\frac{\rho\alpha}{\rho_0 C_p}\frac{\partial I}{\partial z} + K_v\frac{\partial}{\partial z}\theta\frac{\partial \rho\alpha}{\partial z} - K_v\frac{\partial}{\partial z}S\frac{\partial \rho\beta}{\partial z} + K_h\nabla_h\theta\cdot\nabla_h(\rho\alpha) - K_h\nabla_h S\cdot\nabla_h(\rho\beta), \tag{6}$$

with the penetrated shortwave radiation, I, and the potential temperature, θ.

Terms 1–4 in Eq. (2) represent the change in PEA induced by the ocean currents. Terms 1 and 4 represent the PEA advection, including vertical density advection by $\bar{w}$. Term 2, the depth-mean straining, quantifies the change in PEA due to a vertically sheared horizontal current in the presence of a horizontal gradient of vertically averaged density. Term 3, the non-mean straining, represents PEA change due to the

horizontal current and the density with vertically correlated variation. This term dictates that a PEA change may occur due to horizontal change in the vertical density gradient, even if the vertical averaged density is horizontally constant. Term 5 represents a decrease in PEA due to the rearrangement of water in the seasonal boundary layer, induced by vertical mixing. The surface and bottom buoyancy fluxes also contribute to PEA changes (Term 6). An inner sink or source of potential density (Term 7) can contribute to stabilizing or destabilizing of the water column; if a sink (e.g., the penetration of shortwave radiation) is in the upper (lower) half of the water column, PEA will increase (decrease). Term 8 represents change due to divergence/convergence of horizontal eddy diffusive density fluxes and creates a change in the same manner as Term 7. For further explanation of each term and the detailed derivation of Eq. (2), see Burchard and Hofmeister (2008).

Considering the spatiotemporal scales of interest to this study, we simplified the time-dependent equation for PEA under the following assumptions. The vertical velocity in the seasonal boundary layer of the horizontally smoothed fields is quite small (typically on the order of 10^{-6} m s^{-1}). Term 4 of Eq. (2), therefore, becomes one or two orders of magnitude smaller than other terms (e.g., an order of magnitude smaller than Term 3). Likewise, the seasonal contribution from horizontal eddy diffusivity is expected to be small in large-scale averaged fields, except near the equatorial and western boundary current regions (Moisan and Niiler 1998; Giglio and Roemmich 2014; Ren and Riser 2009). In addition, since the vertical density gradient is generally small at the annual maximum of ML depth, we can assume that the bottom buoyancy flux due to vertical mixing (P_b^H) is negligible. For convenience, we assume that only the penetration of shortwave radiation into seawater is solely responsible for the inner source of potential density term (Term 7). With these assumptions, Eq. (2) can be rewritten as follows:

$$\frac{\partial \phi}{\partial t} = \underbrace{-\nabla_h \cdot (\bar{\boldsymbol{u}}\phi)}_{\mathrm{A}} + \underbrace{\frac{g}{H}\nabla_h \bar{\rho} \cdot \int_{-H}^{0} z\tilde{\boldsymbol{u}}\, dz}_{\mathrm{B}} \underbrace{-\frac{g}{H}\int_{-H}^{0}\left(-\frac{H}{2}-z\right)\tilde{\boldsymbol{u}}\cdot\nabla_h\tilde{\rho}\, dz}_{\mathrm{C}} \underbrace{-\frac{\rho_0}{2}P_b^s}_{\mathrm{D}} + \underbrace{\frac{g}{H}\int_{-H}^{0}\left(-\frac{H}{2}-z\right)\left(-\frac{\rho\alpha}{\rho_0 C_p}\frac{\partial I}{\partial z}\right)dz}_{\mathrm{E}} + (Residual), \tag{7}$$

where the residual term includes vertical mixing (Term 5 of Eq. 2) and all terms that are assumed to be negligibly small.

To estimate the vertical profile of penetrating shortwave radiation, $I(z)$, we adopted a generalized empirical model using the inherent optical properties of seawater (Lee et al. 2005). Specifically, the penetration of shortwave radiation is represented as;

$$I(z) = I(0)e^{-K_{VIS}z}, \tag{8}$$

where K_{VIS} is the attenuation coefficient for the visible domain of shortwave radiation and is modeled as a function of depth and absorption and backscattering coefficients at 490 nm (a, b_b, respectively):

$$K_{VIS}(z, a, b_b) = K_1(a, b_b) + \frac{K_2(a, b_b)}{(1+z)^{0.5}}$$

$$K_1(a, b_b) = \chi_0 + \chi_1 a^{0.5} + \chi_2 b_b$$

$$K_2(a, b_b) = \zeta_0 + \zeta_1 a + \zeta_2 b_b.$$

Here, $\chi_0 - \chi_2$ and $\zeta_0 - \zeta_2$ are constant parameters derived from radiative transfer numerical simulations. The typical

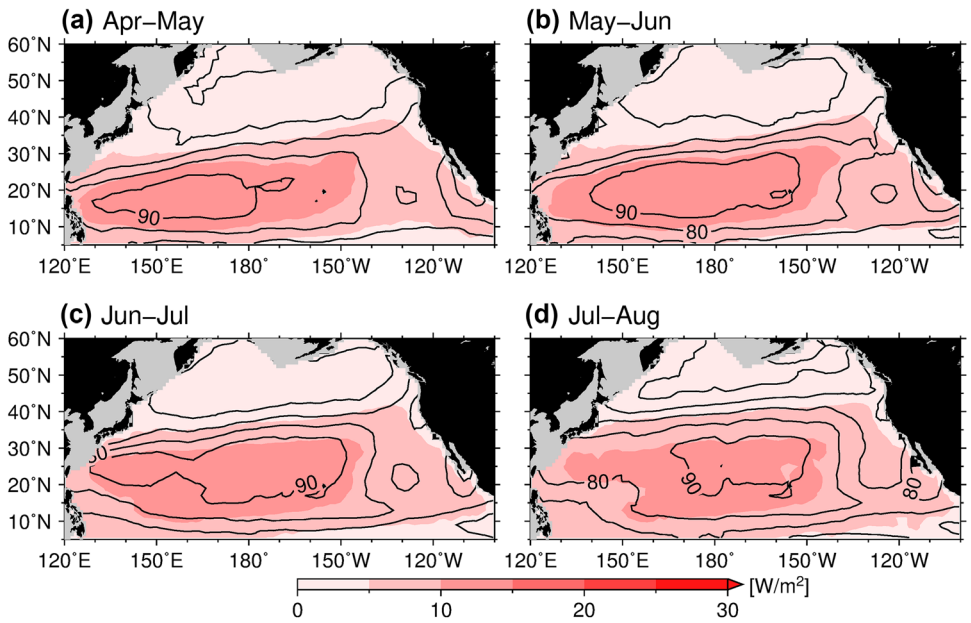

Fig. 7 Spatial distribution of the penetrating shortwave radiation (W m^{-2}) at 40 m depth (color) and at the surface (black contours) for **a** April–May, **b** May–June, **c** June–July, and **d** July–August. Positive values indicate a downward flux

range of K_{VIS}^{-1} is roughly 5–15 m at 10 m depth, with the value increasing with depth and reaching $K_{VIS}^{-1}=25$ m at 100 m depth. The skill and robustness of this model in reproducing the observed transmittance of shortwave radiation for both open oceanic clear water and coastal turbid water have been demonstrated in recent studies (Xiu and Chai 2014; Zoffoli et al. 2017). Figure 7 shows the penetrating component of the shortwave radiation, calculated using the attenuation and backscattering coefficients from the Moderate Resolution Imaging Spectroradiometer (MODIS Aqua; NASA Goddard Space Flight Center, Ocean Ecology Laboratory, Ocean Biology Processing Group 2014). The penetrating component of shortwave radiation has a large spatial variability and becomes larger within the subtropical gyre because of the high transparency of seawater (Fig. 7). The fraction of shortwave radiation able to penetrate beyond the upper few centimeters of the ocean, γ, is assigned a value of 0.33 (Chen et al. 1994; Zhang et al. 2011). The penetrating component of the shortwave radiation at the surface is, $I(0)=\gamma Q_{SW}$, and the non-penetrating buoyancy flux (Fig. 8; i.e., the fraction absorbed near the surface; the sum of sensible and latent heat fluxes, the longwave radiation flux, and the remaining shortwave radiation flux) becomes

$$P_b^s=-g\left(\frac{\alpha\left((1-\gamma)Q_{SW}+Q_{LW}+Q_{SH}+Q_{LH}\right)}{C_p\rho_0}-\beta(E-P)S_0\right). \quad (9)$$

On the spatiotemporal scales relevant to this work, the horizontal velocity vector in Eq. (7) is simply given as the sum of geostrophic and Ekman components. To obtain the vertical profile of Ekman velocity, we assumed that the Ekman velocity is constant in the ML and exponentially decays below the ML, following the Large Eddy Simulation (LES) study of Goh and Noh (2013). By vertically redistributing the Ekman transport estimated from satellite wind fields, we calculated the vertical profiles of Ekman velocity at each grid points. Adding the geostrophic velocity computed from the RG Argo data (using a reference pressure of 1975 dbar) to the Ekman velocity, we obtained the depth-dependent horizontal velocity field. A comparison at 15 m depth between the resulting velocity field and a two-dimensional ocean current product (Ocean Surface Currents Analyses Real-time (OSCAR); Bonjean and Lagerloef 2002) demonstrated a good agreement for both the magnitude and direction of the velocity field (figure not shown).

4.2 PEA balance in the budget

The results of the PEA budget (RHS of Eq. 7) for July–August are shown in Fig. 9. As expected from the phase relationship between PEA development and surface buoyancy forcing (Fig. 6), terms representing atmospheric buoyancy forcing (Terms D and E) are dominant. The sum of the non-penetrating buoyancy forcing (Term D) and the penetration of shortwave radiation (Term E) determines the spatial distribution of PEA development (Fig. 5). Although spatial distribution of the Term D directly reflects that of the non-penetrating buoyancy forcing (Fig. 8d), Term E depends also on the annual maximum of mixed layer depth (H; Fig. 3). According to form of Term E in Eq. (7), the contribution of Term E is larger in the region where the H is extremely deep such as the Kuroshio recirculation region, compared to the regions of the same latitudes where the amount of the penetrative heating (Fig. 7d) is similar.

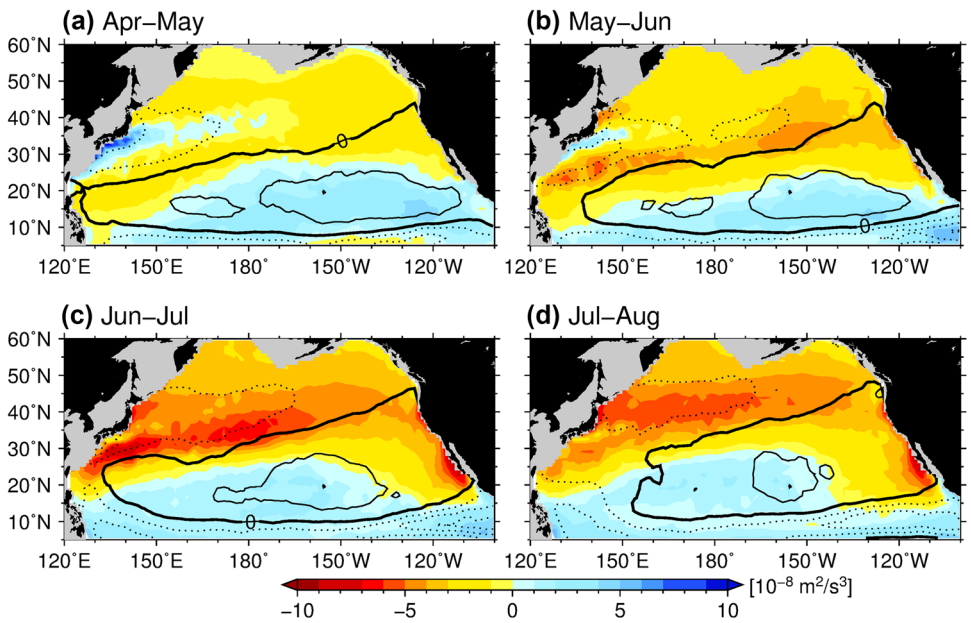

Fig. 8 Spatial distribution of heat (color shade; first term of RHS in Eq. 9) and freshwater (black contours; second term of RHS in Eq. 9) components of the surface non-penetrating buoyancy flux (10^{-8} m^2 s^{-3}) for **a** April–May, **b** May–June, **c** June–July, and **d** July–August. Solid (dash) lines indicate positive (negative) values and the contour interval is 1×10^{-8} m^2 s^{-3}. The negative values indicate net ocean buoyancy gain

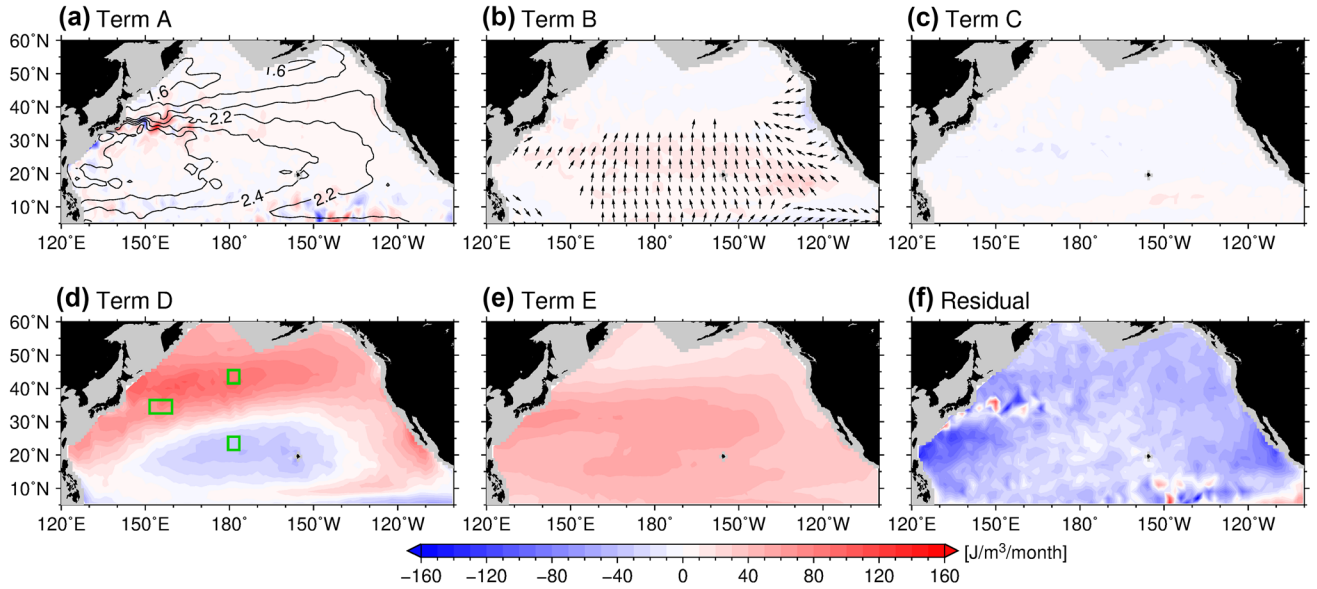

Fig. 9 Spatial distribution of the contributions to the PEA budget in Jul–Aug: **a** PEA advection term overlain by the mean dynamic height (dyn-m; contours); **b** depth-mean straining term with Ekman current vectors at 10 m depth (shown for values larger than 3 m s^{-1} and with constant vector length); **c** non-mean straining term; **d** non-penetrating buoyancy flux term; **e** penetrating shortwave radiation term; **f** residual term. Green boxes in **d** indicate the locations discussed in Sect. 5 (Figs. 12, 13)

Contributions from lateral processes (Terms A, B, and C) are relatively small throughout the period of PEA development (shown in Fig. 9a–c). PEA advection (Term A), however, makes a significant contribution in regions where dynamic height contours are concentrated, such as the Kuroshio/Kuroshio extension and the equatorial current system south of 10°N (Fig. 9a). The depth-mean straining term (Term B) increases PEA up to 30 J m^{-3} $month^{-1}$ south of 30°N. This is because the northward Ekman flow due to the trade winds carries near surface lighter water from the south, which strengthens stratification (Fig. 9b). In the region where the depth-mean straining term reaches its maximum value (approximately 130°W, 20°N), its contribution is comparable to the buoyancy terms. The non-mean straining term (Term C) is smaller than 10 J m^{-3} $month^{-1}$ for the whole of the North Pacific, except in a few limited regions (Fig. 9c).

The residual term shows relatively uniform negative values, suggesting a decrease in PEA due to vertical mixing in the water column. In many parts of the North Pacific, the residual term is the second largest, after the sum of buoyancy flux terms (Fig. 9f). The dominance of Terms D and E in determining the PEA development is also found during other months of the PEA development period (not shown). Accordingly, this suggests, except in the strong current regions, seasonal stratification in the North Pacific develops under a vertical one-dimensional energy balance between the surface and/or inner buoyancy gain and buoyancy redistribution by vertical mixing.

4.3 Residual term and validation of the budget

Although the negative residual term suggests vertical mixing acts to decrease PEA, the term is itself a combination of terms that we are unable to estimate and the errors in those we can estimate. It is difficult to estimate precisely these uncertainties. However, we can get an estimate for the vertical diffusivity by assuming the case that vertical mixing dominates the residual term.

Assuming the vertical mixing (Term 5 of Eq. 2) is responsible for the change in PEA due to residual terms, the vertically averaged vertical diffusivity weighted by the vertical density gradient, $\overline{K_v}$, can be computed as

$$\overline{K_v} = \frac{H}{g}(Residual)\left(\int_{-H}^{0} \frac{\partial \rho}{\partial z} dz\right)^{-1}. \tag{10}$$

The seasonal change in the spatial distribution of $\overline{K_v}$ obtained from each monthly residual term, excluding regions with a positive residual (i.e., with negative $\overline{K_v}$), is shown in Fig. 10. The largest diffusivity value (exceeding 3×10^{-4} m^2 s^{-1}) are found in regions where the ML is relatively deep, and where strong vertical mixing remains into the spring and early summer (Fig. 10a; see also Fig. 4). In mid-summer when the ML becomes shallow relative to H, the diffusivities range roughly between 5×10^{-5} m^2 s^{-1} and 5×10^{-4} m^2 s^{-1}, and show a distinct seasonal change.

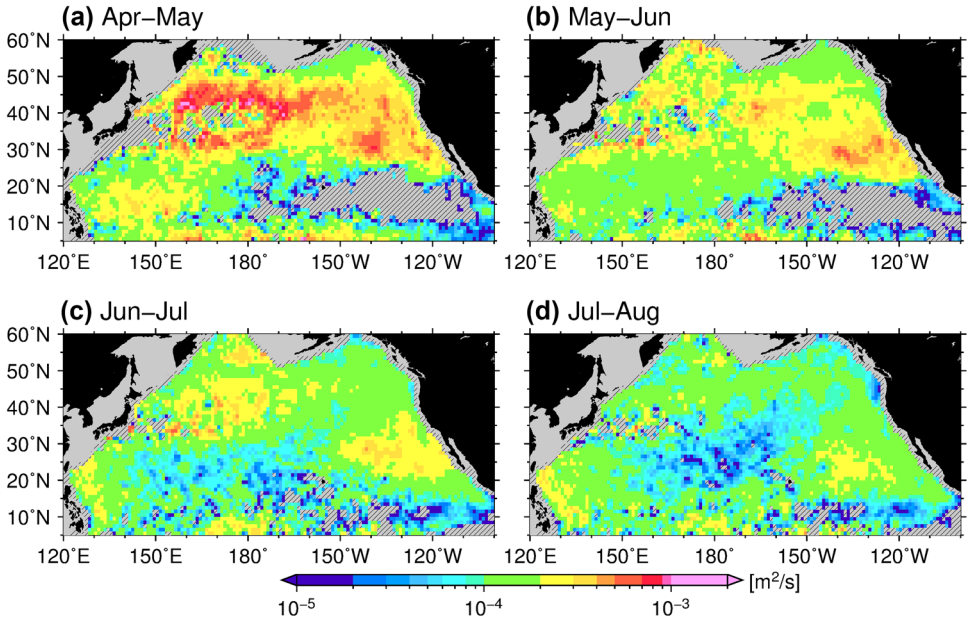

Fig. 10 Spatial distribution of depth-averaged vertical diffusivity, $\overline{K_v}$ ($m^2\ s^{-1}$), for **a** April–May, **b** May–June, **c** June–July, and **d** July–August. Gray hatching indicates regions with positive residuals

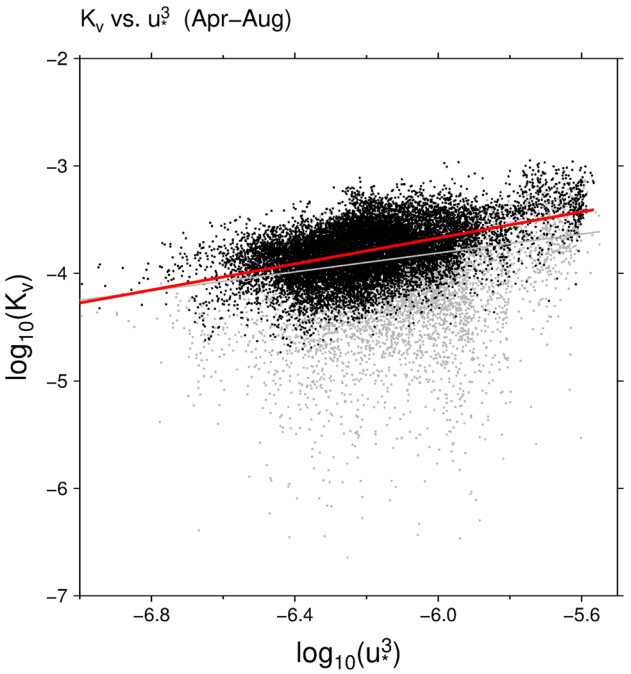

Fig. 11 Scatter plot of the logarithm of depth-averaged vertical diffusivity, $\overline{K_v}$, and the logarithm of the cube of frictional velocity, u_*, for April–August. Data points with a corresponding PEA residual term greater than -20 J m^{-3} $month^{-1}$ are shown in gray. The gray line is the least squares fit for all data points, whereas the red line is the least squares fit for data points colored black

The dependency of the diffusivity on the local wind forcing is shown in a scatter plot of the logarithm of $\overline{K_v}$ and the logarithm of the cube of the surface frictional velocity, $u_* = \sqrt{\tau/\rho}$, where τ is surface wind stress from the daily QuikSCAT and ASCAT products (Fig. 11). $\overline{K_v}$ is significantly correlated with u_*^3 with a correlation coefficient $R = 0.41$ ($p < 0.01$). This correlation is increased ($R = 0.54$; $p < 0.01$) if data points where the corresponding value of the PEA residual is larger than -20 J m^3 $month^{-1}$ are excluded (20 J m^{-3} $month^{-1}$ is roughly equivalent to an error in Q_{net} of 30 W m^{-2}).

Except for low diffusivity in the central North Pacific, estimated summertime diffusivities in the seasonal boundary layer are consistent with values derived from the budget analyses of potential vorticity ($2–5 \times 10^{-4}$ $m^2\ s^{-1}$; Qiu et al. 2006), dissolved oxygen (1.7×10^{-4} $m^2\ s^{-1}$; Sukigara et al. 2011) and heat and salt ($1–3 \times 10^{-4}$ $m^2\ s^{-1}$; Cronin et al. 2013; Cronin et al. 2015) in the northwestern Pacific subtropical recirculation gyre and the northeastern subpolar gyre. Moreover, the gradual decrease in diffusivity as stratification below the ML develops toward late summer is consistent with the result of Cronin et al. (2015).

Good agreement between diffusivities estimated in this work and estimates from previous studies indicated that the residual in the PEA budget is associated mainly with the vertical mixing term, suggesting in turn that the assumptions made to estimate the RHS of Eq. (7) are valid. However, it is to be noted again that this estimated $\overline{K_v}$ include various uncertainties, such as the error in estimates of the surface buoyancy flux. Indeed, the positive residual values shown in Fig. 10 cannot be explained through the vertical mixing process. As a possible cause, contributions from time-varying currents on shorter time scale than monthly and smaller spatial scale than $1° \times 1°$ might be underestimated in the strong current regions, such as the western boundary and equatorial current system (c.f., Fig. 9a–c).

Indeed, the importance of time-varying currents in contributing to the upper ocean heat content changes has been emphasized by several previous studies focusing on the Kuroshio Extension region (e.g., Qiu and Kelly 1993; Vivier et al. 2002).

5 Discussion

Seasonal stratification in the North Pacific develops under a vertical one-dimensional energy balance, except in regions with strong current (Fig. 9) and it is suggested that the development of seasonal stratification is strongly associated with the seasonal cycle of buoyancy forcing (Fig. 6). In this chapter, we examine the detail of the local PEA balance to reveal the relative contributions of oceanic lateral processes, and to investigate the influences of difference in the composition of atmospheric buoyancy forcing.

We set a box in the Kuroshio extension region (150–160°E, 32–37°E; box KE) to demonstrate the relative importance and role of the lateral processes on the PEA development. And, in order to show the influences of difference in the composition of atmospheric buoyancy forcing, we choose the other two boxes which have similar accumulated ocean buoyancy gains during the warming season (box P: 179°E–176°W, 40°–45°N; box

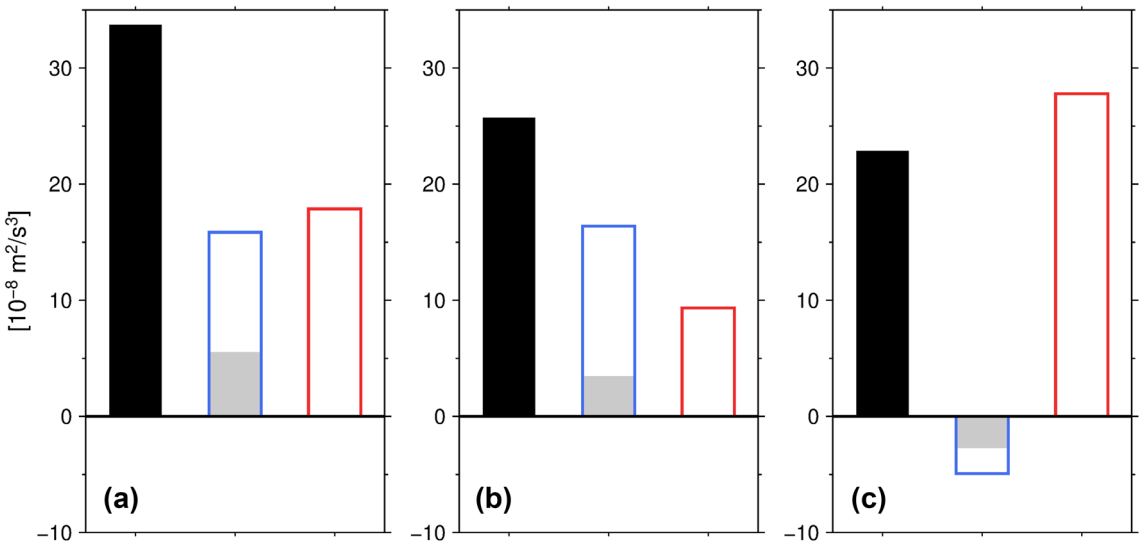

Fig. 12 Accumulated April–August oceanic buoyancy gain (10^{-8} m^2 s^{-3}; black bars) and its components for the **a** box KE, **b** box P, and **c** box N. The blue (red) bars indicate non-penetrating (penetrating) components of oceanic buoyancy gain. Gray bars within blue bars show the freshwater component of the non-penetrating buoyancy gain

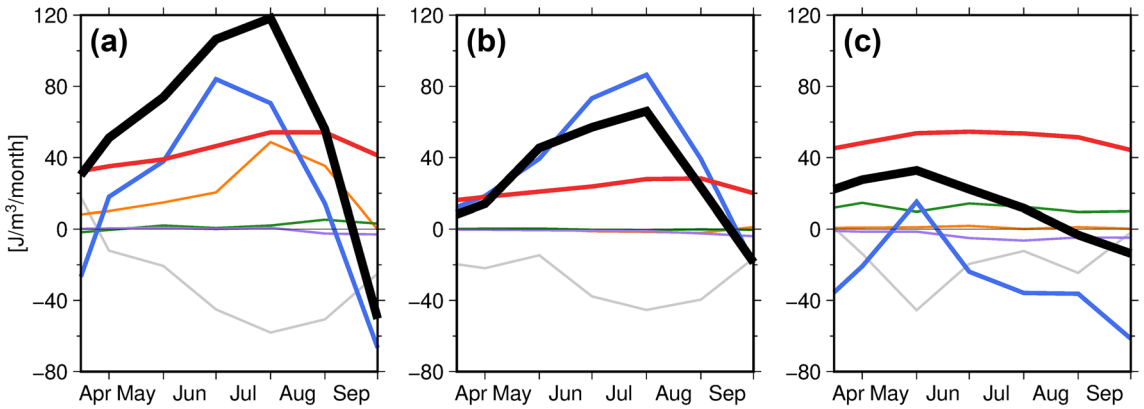

Fig. 13 April–September time series of the time rate change in PEA (J m^{-3} month^{-1}; black line) and each term in the PEA budget (Eq. 7) for the **a** box KE, **b** box P, and **c** box N. Terms shown are the PEA advection term (orange line), the depth-mean straining term (green line), the non-mean straining term (purple line), the non-penetrating buoyancy flux term (blue line), the penetrating shortwave radiation term (red line), and the residual term (gray line)

N: 179°E–176°W, 20°–25°N). Averaged over each region, August PEA is 196.6 J m^{-3} for the box P, 128.9 J m^{-3} for the box N, and 383.0 J m^{-3} for the box KE (c.f. Fig. 2).

The accumulated ocean buoyancy gain and its composition for the three regions are shown in Fig. 12. The latter two regions have similar values of the accumulated ocean buoyancy gains during the development phase of the seasonal stratification but, their compositions are quite different. The penetrating shortwave radiation and the non-penetrating components are both positive in the box P. On the other hand, in the box N, the non-penetrating component is negative (i.e. ocean buoyancy loss), mainly due to strong evaporation and thus latent heat cooling in the subtropical region.

Figure 13 shows the time series of the PEA budget averaged over each region. Only in the box KE does PEA advection play a significant role in the development of seasonal stratification (Fig. 13a). Since higher PEA waters are carried into the region from upstream of the Kuroshio current, the PEA advection term also peaks late in the developing phase. As a result, PEA development peaks 1 month later than the buoyancy gain. In August, PEA advection contributes to ~41% of the time rate change in PEA.

Comparing the box P and box N (Fig. 13b, c), the PEA budgets show a fundamental difference in the balance, although their net buoyancy gains are similar. In the box P, the dominant contribution from the non-penetrating buoyancy flux (Term D in Eq. 7) controls the seasonal cycle, and the penetrating shortwave radiation term (Term E) and the vertical mixing term (residual) are nearly balanced. On the other hand, in the box N, since the non-penetrating buoyancy term is negative (except for June), the PEA cannot increase through the warming season as it does in the box P. Note that the negative non-penetrating buoyancy term at the surface here does not imply vertical mixing within the surface layer.

Since the relative size of the residual term (assumed to be the contribution of vertical mixing) to the time rate of change in PEA is not significantly different between the box P and the box N, this difference in the PEA term balance is attributed to the difference in the component of buoyancy forcing, rather than the local vertical mixing intensity. That is, even if the total buoyancy gain would be same, a condition that the non-penetrating component also contributes to the total buoyancy gain—as is the case in the North Pacific except for the subtropical central North Pacific (Fig. 9d)—is more favorable for the formation of more intense PEA stratification. These results emphasize the important influence of the "composition" of buoyancy forcing, in addition to the "total magnitude", on the development of seasonal stratification.

6 Summary

Based on the Argo profile data and atmospheric buoyancy/momentum flux data derived mainly from satellite observations, we investigated the development of the seasonal stratification in the North Pacific. Applying the concept of PEA, which has historically been used in studies of coastal and shelf seas (e.g. Gronholz et al. 2017), to the seasonal stratification of the open ocean, we have quantitatively described the development of the seasonal stratification. Using PEA as a metric to represent the stratification, and by analyzing its budget, we have estimated the contribution of lateral processes and vertical mixing as the residual. Both contributions would have been difficult to quantify from observational data by using other previous metrics.

The PEA budget analysis shows that the seasonal stratification develops under a vertical one-dimensional energy balance between the atmospheric buoyancy forcing and the vertical mixing in the water column over a large part of the North Pacific, except for the Kuroshio/Kuroshio Extension and equatorial current system south of 10°N. In the Kuroshio Extension region, a significant part of the time rate of change in PEA can be attributed to the advection of PEA. A comparison of PEA term balance indicates that the condition that both of the non-penetrating and penetrating forcing contribute is important for the development of more stable stratification in the North Pacific. It is worth emphasizing that not only "How large amount of the heat enters the ocean" but also "How to heat the ocean" is important for forming the upper ocean stability during the warming season that affects the physical and biogeochemical processes through controlling the vertical mixing.

The vertical diffusivity, depth-averaged over the seasonal boundary layer and estimated from the residual of the energy budget, ranging from 5×10^{-5} m^2 s^{-1} to 5×10^{-4} m^2 s^{-1}. This range is consistent with previous indirect estimates for other independent tracers (e.g., potential vorticity), which gives us confidence in these estimates. The diffusivity shows significant spatial and seasonal variability, indicative of its dependence on the strength of local wind forcing during the warming season.

Pertinent to the discussion of vertical mixing under a stabilizing buoyancy force, recent observational and LES studies have shown that the oceanic response to wind forcing is latitude-dependent, due to the Coriolis parameter (Goh and Noh 2013; Lee et al. 2015; Yoshikawa 2015). Moreover, modeling studies have demonstrated that the wind energy input to near-inertial motion contributes to the near-surface mixing (Furuichi et al. 2008; Jochum et al. 2013). In this study, the contributions from the directly wind-induced mixing and the mixing associated

with the near-inertial energy are included in the residual term of the PEA budget. It is difficult, however, to identify the mechanisms responsible for the vertical mixing due to its large uncertainty and errors from other terms. Further studies are thus needed to explain quantitatively the spatial distribution of the vertical diffusivity in the seasonal boundary layer and its impact on the sea surface temperature development and biogeochemical processes during the warming season.

Acknowledgements We acknowledge the JAMSTEC Argo team for providing the quality-controlled Argo profiles (http://www.jamstec.go.jp/ARGO/argo_web/ancient/AQC/index.html). Surface heat flux products were provided by J-OFURO3 (https://j-ofuro.scc.u-tokai.ac.jp/en/). ASCAT data are produced by the Centre de Recherche et d'Exploitation Satellitaire at Institut français de recherche pour l'exploitation de la mer, Plouzané (France), and QuikSCAT data are produced by Remote Sensing Systems and sponsored by the NASA Ocean Vector Winds Science Team (available at http://www.remss.com).

Funding R. Y. is a research fellow of the Japan Society for the Promotion of Science (JSPS) and is financially supported through JSPS Grant 17J02314. R.Y. also acknowledges support from the International Joint Graduate Program in Earth and Environmental Science (GP-EES) and Tohoku University Division for Interdisciplinary Advanced Research and Education. T. S. is financially supported by JSPS through Grants 16H04046 and 15H02129.

Compliance with ethical standards

Conflict of interest The authors declare that they have no conflict of interest.

References

Akima H (1970) A new method of interpolation and smooth curve fitting based on local procedures. J Assoc Comput Mach 17:589–602. https://doi.org/10.1145/321607.321609

Argo (2000) Argo float data and metadata from Global Data Assembly Centre (Argo GDAC). SEANOE. http://doi.org/10.17882/42182

Bonjean F, Lagerloef GSE (2002) Diagnostic model and analysis of the surface currents in the tropical Pacific Ocean. J Phys Oceanogr 32:2938–2954. https://doi.org/10.1175/1520-0485(2002)032%3c2938:DMAAOT%3e2.0.CO;2

Burchard H, Hofmeister R (2008) A dynamic equation for the potential energy anomaly for analysing mixing and stratification in estuaries and coastal seas. Estuar Coast Shelf Sci 77:679–687. https://doi.org/10.1016/j.ecss.2007.10.025

Capotondi A, Alexander MA, Bond NA, Curchitser EN, Scott JD (2012) Enhanced upper ocean stratification with climate change in the CMIP3 models. J Geophys Res Oceans 117:C04031. https://doi.org/10.1029/2011JC007409

Chen D, Busalacchi AJ, Rothstein LM (1994) The roles of vertical mixing, solar radiation, and wind stress in a model simulation of the sea surface temperature seasonal cycle in the tropical Pacific Ocean. J Geophys Res Oceans 99:20345–20359. https://doi.org/10.1029/94JC01621

Cronin MF, Bond NA, Farrar JT, Ichikawa H, Jayne SR, Kawai Y, Konda M, Qiu B, Rainville L, Tomita H (2013) Formation and erosion of the seasonal thermocline in the Kuroshio Extension recirculation gyre. Deep Sea Res II 85:62–74. https://doi.org/10.1016/j.dsr2.2012.07.018

Cronin MF, Pelland NA, Emerson SR, Crawford WR (2015) Estimating diffusivity from the mixed layer heat and salt balances in the North Pacific. J Geophys Res Oceans 120:7346–7362. https://doi.org/10.1002/2015JC011010

Furuichi N, Hibiya T, Niwa Y (2008) Model-predicted distribution of wind-induced internal wave energy in the world's oceans. J Geophys Res Oceans 113:C09034. https://doi.org/10.1029/2008JC004768

Giglio D, Roemmich D (2014) Climatological monthly heat and freshwater flux estimates on a global scale from Argo. J Geophys Res Oceans 119:6884–6899. https://doi.org/10.1002/2014JC010083

Goh G, Noh Y (2013) Influence of the Coriolis force on the formation of a seasonal thermocline. Ocean Dyn 63:1083–1092. https://doi.org/10.1007/s10236-013-0645-x

Gronholz A, Gräwe U, Paul A, Schulz M (2017) Investigating the effects of a summer storm on the North Sea stratification using a regional coupled ocean-atmosphere model. Ocean Dyn 67:211–235. https://doi.org/10.1007/s10236-016-1023-2

Hosoda S, Nonaka M, Tomita T, Taguchi B, Tomita H, Iwasaka N (2015) Impact of downward heat penetration below the shallow seasonal thermocline on the sea surface temperature. J Oceanogr 46:1–16. https://doi.org/10.1007/s10872-015-0275-7

Huffman GJ, Adler RF, Morrissey MM, Bolvin DT, Curtis S, Joyce R, McGavock B, Susskind J (2001) Global precipitation at one-degree daily resolution from multisatellite observations. J Hydrometeor 2:36–50. https://doi.org/10.1175/1525-7541(2001)002%3c0036:GPAODD%3e2.0.CO;2

Jochum M, Briegleb BP, Danabasoglu G, Large WG, Norton NJ, Jayne SR, Alford MH, Bryan FO (2013) The impact of oceanic near-inertial waves on climate. J Clim 26:2833–2844. https://doi.org/10.1175/JCLI-D-12-00181.1

Johnston TMS, Rudnick DL (2009) Observations of the transition layer. J Phys Oceanogr 39:780–797. https://doi.org/10.1175/2008JPO3824.1

Kako S, Kubota M (2007) Variability of mixed layer depth in Kuroshio/Oyashio Extension region: 2005–2006. Geophys Res Lett 34:L11612. https://doi.org/10.1029/2007GL030362

Lee Z, Du K, Arnone R, Liew S, Penta B (2005) Penetration of solar radiation in the upper ocean: a numerical model for oceanic and coastal waters. J Geophys Res Oceans 110:C09019. https://doi.org/10.1029/2004JC002780

Lee E, Noh Y, Qiu B, Yeh S-W (2015) Seasonal variation of the upper ocean responding to surface heating in the North Pacific. J Geophys Res Oceans 120:5631–5647. https://doi.org/10.1002/2015JC010800

Maes C, O'Kane TJ (2014) Seasonal variations of the upper ocean salinity stratification in the Tropics. J Geophys Res Oceans 119:1706–1722. https://doi.org/10.1002/2013JC009366

Moisan JR, Niiler PP (1998) The seasonal heat budget in the North Pacific: net heat flux and heat storage rates (1950–1990). J Phys Oceanogr 28:401–420. https://doi.org/10.1175/1520-0485(1998)028%3c0401:TSHBOT%3e2.0.CO;2

Monterey G, Levitus S (1997) Seasonal variability of mixed layer depth for the world ocean. NOAA Atlas NESDIS 14, U.S. Gov. Printing Office, Washington, DC

NASA Goddard Space Flight Center, Ocean Ecology Laboratory, Ocean Biology Processing Group (2014) Moderate-resolution Imaging Spectroradiometer (MODIS) Aqua Inherent Optical Properties Data; 2014 Reprocessing. NASA OB. DAAC, Greenbelt. https://doi.org/10.5067/AQUA/MODIS/L3B/IOP/2014

Oka E, Qiu B, Takatani Y, Enyo K, Sasano D, Kosugi N, Ishii M, Nakano T, Suga T (2015) Decadal variability of subtropical mode water subduction and its impact on biogeochemistry. J Oceanogr 71:389–400. https://doi.org/10.1007/s10872-015-0300-x

Qiu B, Chen S (2006) Decadal variability in the formation of the North Pacific subtropical mode water: oceanic versus atmospheric control. J Phys Oceanogr 36:1365–1380. https://doi.org/10.1175/JPO2918.1

Qiu B, Kelly KA (1993) Upper ocean heat balance in the Kuroshio Extension region. J Phys Oceanogr 23:2027–2041. https://doi.org/10.1175/1520-0485(1993)023%3c2027:UOHBIT%3e2.0.CO;2

Qiu B, Chen S, Hacker P (2004) Synoptic-scale air-sea flux forcing in the western North Pacific: observations and their impact on SST and the mixed layer. J Phys Oceanogr 34:2148–2159. https://doi.org/10.1175/1520-0485(2004)034%3c2148:SAFFIT%3e2.0.CO;2

Qiu B, Hacker P, Chen S, Donohue KA, Watts DR, Mitsudera H, Hogg NG, Jayne SR (2006) Observations of the subtropical mode water evolution from the Kuroshio Extension System Study. J Phys Oceanogr 36:457–473. https://doi.org/10.1175/JPO2849.1

Ren L, Riser SC (2009) Seasonal salt budget in the northeast Pacific Ocean. J Geophys Res Oceans 114:C12004. https://doi.org/10.1029/2009JC005307

Roemmich D, Gilson J (2009) The 2004–2008 mean and annual cycle of temperature, salinity, and steric height in the global ocean from the Argo Program. Prog Oceanogr 82:81–100. https://doi.org/10.1016/j.pocean.2009.03.004

Simpson JH (1981) The shelf-sea fronts: implications of their existence and behavior. Philos Trans R Soc Lond A 302:531–546. https://doi.org/10.1098/rsta.1981.0181

Suga T, Motoki K, Aoki Y, MacDonald AM (2004) The North Pacific climatology of winter mixed layer and mode waters. J Phys Oceanogr 34:3–22. https://doi.org/10.1175/1520-0485(2004)034%3c0003:TNPCOW%3e2.0.CO;2

Sukigara C, Suga T, Saino T, Toyama K, Yanagimoto D, Hanawa K, Shikama N (2011) Biogeochemical evidence of large diapycnal diffusivity associated with the subtropical mode water of the North Pacific. J Oceanogr 67:77–85. https://doi.org/10.1007/s10872-011-0008-5

Tomita H, Kako S, Cronin MF, Kubota M (2010) Preconditioning of the wintertime mixed layer at the Kuroshio Extension Observatory. J Geophys Res Oceans 115:C12053. https://doi.org/10.1029/2010JC006373

Tomita H, Hihara T, Kako S, Kubota M, Kutsuwada K (2018) An introduction to J-OFURO3, a third-generation Japanese ocean flux data set using remote-sensing observations. J Oceanogr. https://doi.org/10.1007/s10872-018-0493-x

Vivier F, Kelly KA, Thompson L (2002) Heat budget in the Kuroshio Extension Region: 1993–99. J Phys Oceanogr 32:3436–3454. https://doi.org/10.1175/1520-0485(2002)032%3c3436:HBITKE%3e2.0.CO;2

Xiu P, Chai F (2014) Connections between physical, optical and biogeochemical processes in the Pacific Ocean. Prog Oceanogr 122:30–53. https://doi.org/10.1016/j.pocean.2013.11.008

Yoshikawa Y (2015) Scaling surface mixing/mixed layer depth under stabilizing buoyancy flux. J Phys Oceanogr 45:247–258. https://doi.org/10.1175/JPO-D-13-0190.1

Yu L, Jin X, Weller RA (2008) Multidecade global flux datasets from the objectively analyzed air-sea fluxes (OAFlux) project: latent and sensible heat fluxes, ocean evaporation, and related surface meteorological variables. OAFlux Project Technical Report OA-2008-01. Woods Hole Oceanographic Institution, Woods Hole

Zhang R-H, Chen D, Wang G (2011) Using satellite ocean color data to derive an empirical model for the penetration depth of solar radiation (H_p) in the tropical Pacific Ocean. J Atmos Ocean Technol 28:944–965. https://doi.org/10.1175/2011JTECHO797.1

Zoffoli ML, Lee Z, Ondrusek M, Lin J, Kovach C, Wei J, Lewis M (2017) Estimation of transmittance of solar radiation in the visible domain based on remote sensing: evaluation of models using in situ data. J Geophys Res Oceans 122:9176–9188. https://doi.org/10.1002/2017JC013209